https://doi.org/10.61343/jcm.v2i01.40 ISSN: 2583-9152
Journal of Condensed Matter
Volume 02 Issue 01
Journal homepage: https://jcm.thecmrs.in

Mg Doped ZnO Nanostructures: Application as an Environmental Photo-Catalyst

Shakshi Chauhan[1,a], Jyoti Gahlawat[1], Parveen Bhatt[1], Kaushlya Sihag[2]

[1]*Department of Physics, Baba Mastnath University, Rohtak (Haryana), India*
[2]*Department of Physics, School Education, Panchkula (Haryana), India*

Abstract

In this era, metal oxide nanoparticles with appliances in solar, catalysis, sensors, actuators, and many other fields, are highly sought-after because of their wide band gap. This study examines the Mg doped ZnO nanoparticles for the structural, electrical transportation and photo-catalytic behaviour. The XRD, FT-IR (Infrared Spectroscopy), PL (Photoluminescence), and Complex Impedance Spectroscopy were used to characterise the prepared sample. The wurtzite hexagonal structure in space group P63mc was shown by the XRD data. The analyzed crystallite sizes, planner distances, and cell volumes of Mg doped ZnO nanoparticles are 35.2 nm, 2.6122 Å, and 60.91 Å^3, respectively. The aggregation in sample is visible in the micrographs. The PL spectra was traced at an excitation wavelength of 330 nm (λ) using a PL spectrometer. Using the FTIR approach, IR spectra with acmes about 520–640 cm^{-1} were traced, leading to Zn–O bond stretching. Using a photocatalytic reactor, the photocatalytic degradation of magnesium-doped ZnO nanoparticles was measured for two hours. For the Mg doped ZnO sample, the degradation efficiencies (η%) is 67 percent.

Keywords: Zinc Oxide, Mg, Photo-luminescence, Visible light, Photo-catalytic.

Received 14 November 2023; Received in revised form 28 January 2024; Accepted 04 February 2024

Introduction

A new class of devices, including spin light-emitting diodes, spin field effect transistors, catalytic devices, spin-based quantum computers, and memory systems, is being developed by the combination of heavier spin and charge [1-4]. Because of their potential application in spintronics devices, where the spin and charge of the electrons can be applied mutually, photocatalysis—which is created by doping a semiconductor with a small amount of transition metals - has drawn a lot of attention. In addition, photocatalysis holds promise for a number of technological advancements, including non-volatility, increased data processing speed, lower electronic power utilisation, water purification, and higher integration densities when compared to other semiconductors [2,5]. The implementation of this kind of catalytic application is still a contentious issue because of the material's poor magnetic characteristics. All aspects of Mn-doped II–V and III–V compound semiconductors have been thoroughly studied. For data storage, ferromagnetism at room temperature is one of the most crucial properties. One of the main challenges for semiconductor spintronics devices is the discovery of appropriate magnetic semiconducting materials that will successfully allow spin-polarized carriers to be injected, transported, and modulated. Diluted magnetic semiconductors with cations that match the valence of common magnetic ions like magnesium, such as CdMnTe and ZnMnSe, have been the subject of numerous investigations. The II–VI oxide semiconductor zinc oxide (ZnO) exhibits a straight and broad band gap (3.37 eV), good transparency, long-term stability, and a high exciton binding energy (almost 60 meV at room temperature) [6-12]. It has received careful scrutiny due to its superior optoelectronic, sensing, and photocatalytic characteristics. Numerous technological uses come to an end with it, such as photocatalysts, resistive switching devices, lasers, sensors, light emitting diodes, solar cells, and, most recently, spintronics. Similar to ZnS nanoparticles, it displays strong room temperature luminescence capabilities; however, it might be enhanced by using ZnO/ZnS nanocomposites or the ZnS:Mn/ZnO nanocrystals core shell [6, 12-15]. Numerous techniques, including sol–gel, hydrothermal, chemical synthesis, chemical vapour deposition, thermal evaporation, and others, have been used to produce modified ZnO nanoparticles and thin films. In this study, we looked at how the temperature during calcinations affected the structural, optical, and photocatalytic characteristics of magnesium-modified ZnO.

[a] chauhanshakshi912@gmail.com

Experimental Detail

In the current work, preparatory materials were derived from $Zn(CH_3COO)_2$ (zinc acetate dehydrate), $MgCl_2$ (magnesium chloride), NaOH (Sodium hydroxide), C_2H_5OH (ethanol), and DI water. No additional purification was required. Zinc acetate dehydrate and sodium hydroxide were used as the stoichiometric ratio preparatory precursors or materials for the conformist co-precipitation synthesis of magnesium modified ZnO nanoparticles (referred to as Mg-ZnO (0.04)). After that, these precursors were dissolved in a mixture of DI water and ethanol. After then, the mixture of these precursors was disturbed for a whole hour at 80 °C. This solution was then allowed to place overnight before being repeatedly cleaned with DI water and dried in an oven program to 80 ˚C for 12 hours. The resulting powder was then annealed for four hours at 450 °C and examined using a variety of characterization methods, including photocatalytic tests, XRD, SEM, FTIR, and PL.

Results and Discussion

Structural Analysis

Figure 1 showed the Mg metal doped ZnO sample's XRD pattern. The JCPDS file #80-0075 and the crystal planes of the wurtzite ZnO structure balanced all of the diffraction peaks. The XRD patterns of synthetic samples of Mg substituted ZnO in the range of 2θ (diffraction angle) from 10° to 90° are displayed in Figure 1, which includes all of the diffraction peaks [7]. As indicated by hkl values (100), (002), (101), (102), (103), (200), (112), (201), and (202), etc., the diffraction peaks at 2θ values 31.66°, 34.31°, 36.28°, 47.53°, 56.33°, 62.54°, 67.89°, 69.08°, 72.46°, 76.93°, and 81.48° are depicted in Figure 1.

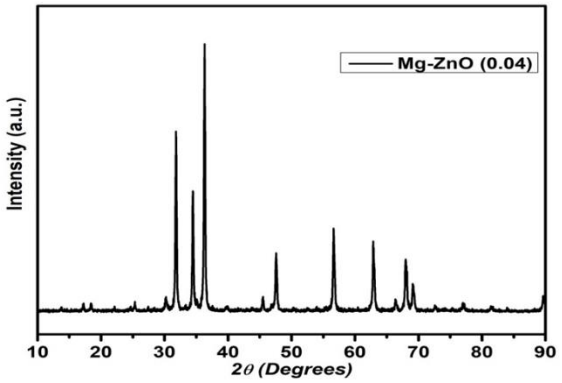

Figure 1: XRD patterns of Mg doped ZnO calcined at 450 ℃.

This demonstrated that dopant magnesium ions effectively substituted Zn^{2+} ions. No signals from secondary doped ion phases or another ZnO phase were detected. The Scherer relation can be used to measure the standard particle grain size (D).

Table 1: Pure zinc oxide with annealing and its lattice parameters

Sample	Crystallite size (nm)	Inter planar spacing (d) Å	lattice constant Å		Volume (V) Å^3	X ray Density (d_x) g/cm^3	Lattice Strain η
			a=b	c			
Mg-ZnO (0.04)	35.2	2.6122	3.5721	5.4247	60.91	8.04	0.0061

The lattice parameter of the samples was computed, and the values of 'd' were ascertained using the Bragg equation. Because of the surface aggregation of ZnO nanoparticles and the amalgamation of Mg into the lattices, the diffraction patterns of the cerium ZnO samples are nearly the same as those of nanoparticles of pure ZnO with a slight adjustment to higher 2θ angles in the peak position. This indicates that iron doping preserves the same orientations of the diffraction plane and does not change the ZnO hexagonal wurtzite structure. Furthermore, in contrast to the spiky and extremely intense peaks for the hexagonal structures, the extremely lower intensities of the diffraction crest assigned to the oxides describe the hexagonal phase of the zinc oxide lattice. Additionally, as reported by numerous other sources [15–18], the crystalline diameters decrease with Mg substitution because of the difference in the ionic radii of Mg and Zn ions. The addition of the magnesium substituent to the lattices allowed for the determination of the change in the lattice variables as measured from the XRD data. For Mg doped ZnO nanoparticles, the lattice variables a and c are 3.5721 Å and 5.4247 Å, respectively (Table 1), which are therefore close to the standards value for undoped Zinc Oxides nanoparticles (Table 1). Additionally, the c/a ratio values have been roughly constant, and they exhibit remarkable consistency with the standard values of 1.60. The Williamsons-Hall (W-H) equation [9] can be used to determine the lattice strains stimulated by the amalgamation of Mg ions into the crystals construction of Mg doped ZnO as well as the crystalline sizes. Since the crystalline sizes and strains are obtained from the Williamsons-Hall graphs, the y-intercepts provide the opposite of the crystalline sizes, and the slopes are equivalent to the strain value. Table 1 compiles the strain values and crystallite scale of zinc oxide nanoparticles, which are determined from W-H plots. Table 1 discloses the estimated cell characteristics of ZnO doped with magnesium.

Morphological Analysis

Figure 2 shows the impact of Mg ion on the morphology of ZnO when clicked out using FeSEM. Because of the massive chemical reaction of energy, the micrographs shown in the illustration are polycrystalline in nature and display agglomeration, asymmetric shapes, and sizes. The asymmetrical particle dispensation ensures that nanostructures have structural, electrical, and other properties. The XRD review also makes these findings accurate [10].

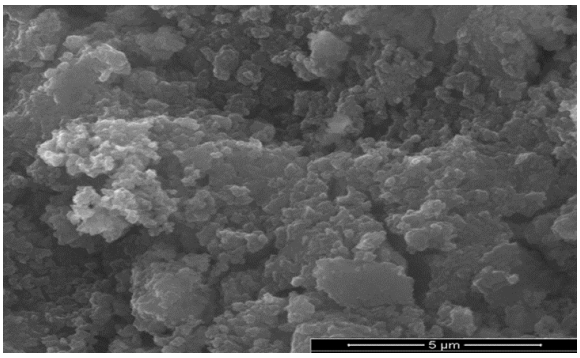

Figure 2: FESEM images of Mg doped ZnO nanoparticles calcined at 450 ℃.

PL Analysis

The photoluminescence (PL) spectra of a Mg doped ZnO sample with a purposeful excitation wavelength (λ) of 330 nm are shown in Figure 3.

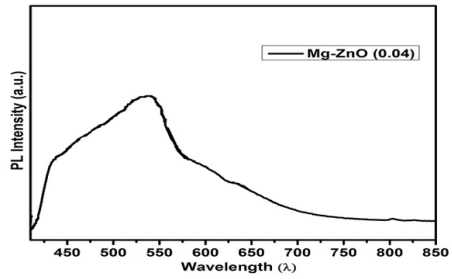

Figure 3: Photoluminescence spectrum of Mg doped ZnO nanoparticles calcined at 450 ℃.

Strong centralization of the emission peak was seen at about 435 nm, with red shifts associated with the close-band emission in zinc oxide. This is because the substitution of magnesium ions results in doped ZnO inadequacies, which may establish a negligible energy level close to the conduction bands. Therefore, the insignificant energy levels generated in the recombination centres might support the violet emissions peaks [10–12]. As a result, the adjustment of Mg led to the formation of interstitial Zn ions and oxygen vacancies, which significantly impacted the optical properties of the doping ion-modified ZnO samples.

FT-IR Analysis

The 400–4000 cm^{-1} wave range FTIR spectra of the magnesium doped ZnO sample is displayed in Figure 4.

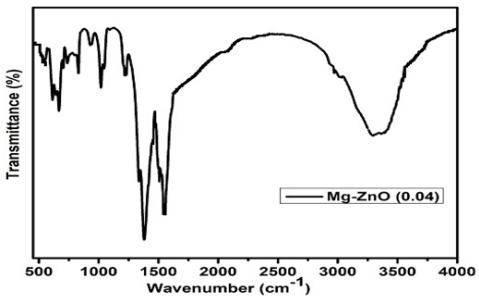

Figure 4: FT-IR Spectrum of Mg doped ZnO nanoparticles calcined at 450 ℃.

The IR pinnacles of the magnesium-doped ZnO samples are located at 3422, 2403, 1600, 1434, 1232, 843, 622, and 535 cm^{-1}. The vibrations of the C-H, C=O, and C-O bonds are represented by the FTIR peak in the range of 680 cm^{-1} to 1600 cm^{-1}. The small and jumbled absorptions band at around 843 cm^{-1} accounts for the sparse situation next to Mg in the Zn-O lattice structure. The elongation of the Zn-O bonds is reflected in peaks about 535–680 cm^{-1} [12]. The remaining peaks, which represent the O=C=O bond availabilities, submerged water mode of bending, and stretching vibrations of the O-H bond, are located between 1600 and 3422 cm^{-1}.

Photo-catalytic Test

The prepared Mg doped ZnO sample was analysed for photo-catalysis applications. The photo-catalysis experiments were conducted for the degradation of MB (methylene blue) and Malathion pesticide, in an aqueous medium in the presence of visible light. In this study, the catalytic reactor structure was set in a cubical chamber for the accomplishment of a dark medium. In a typical procedure, 50 mL of dye solution (12 mg/L) was put in a container, containing photo-catalyst (1.1 g/L). After 20 minutes of sonication, the powdered photocatalyst was fully distributed throughout the dye solution. Following this, the solution was left in the dark for 30 minutes to establish equilibrium between dye and catalyst [13]. After continuous time intervals of 20 minutes during the test run, 2–3 mL of the solution was removed and centrifuged to remove the photo-catalyst for the prescription of the dye concentration in solution using a UV-visible spectrophotometer.

Photo-catalytic studies

As said in segment 3.5, the degradation spectra of the MB dye in an aqueous solution was observed when visible light was applied in order to study the photo-catalytic investigations of the Mg doped ZnO sample. Because of the long chromophore, the distinctive absorption peaks of MB dye are situated at approximately 662 nm. The breakdown of MB (organic pollutant) dye in the medium of a ZnO

sample doped with magnesium as a photo-catalyst is shown in Figure 5 with respect to time variations.

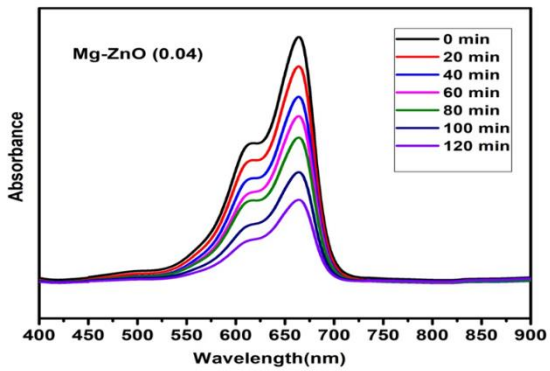

Figure 5: Photo-catalytic degradation spectrum of Mg doped ZnO nanoparticles calcined at 450℃.

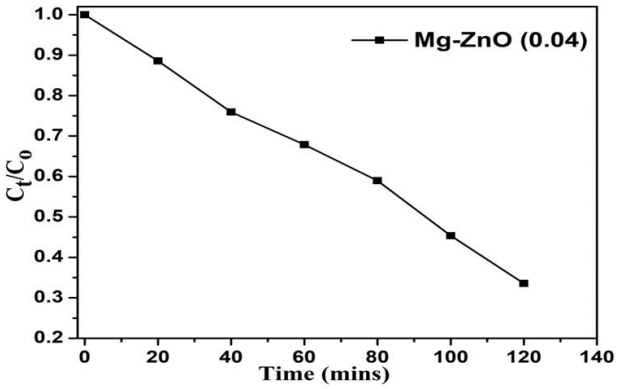

Figure 6: Variation of Ct/Co (concentration ratio) with time (min) for Mg doped ZnO nanoparticles calcined at 450 ℃

Figures 5 and 6 show how the amount of organic contaminants in water decreases, giving way to the catalyst's shape and the dye's atomic structure, among other things. Based on the relation [23-25], the efficiencies of degradation (η) of the BCFO photocatalysts have been estimated:

$$Degradation\ (\eta\%) = \frac{C_o - C_t}{C_o} * 100$$

where C_t is the absorbance intensity at time t = t and C_o is the initial absorbance intensity. Figure displays the changes in the comparative rates (C_t/C_o) of the ZnO sample doped with magnesium. Since the MB dye does not absorb light at a higher rate, we need a photo-catalyst nanomaterial to absorb light at unusual wavelengths (λ) in order to degrade the MB dye and remove organic contaminants from water [15, 18]. In comparison to ZnO and many other catalysts, such as Ce-ZnO/ZnO, Ce-TiO_2/TiO_2, etc., the energy gap modification in the doped ZnO sample due to the doping of Mg is enhanced the surface reactivity because of augmenting in surface area and well crystalline character [17, 19-20]. This reveals preferential catalysis practice under the visible light irradiation.

Photo-catalytic Mechanism

The presence of a possible catalyst, such as Mg-doped ZnO, is necessary to understand the process of photon-induced catalysis and to identify the precise mechanism involved in visible light-driven photocatalysis. Because of light absorption, light irradiation (hν ≥ Eg) on the photo-catalyst surface produces electrons-holes (e^- - h^+) in the band structure, which is crucial for the degradation of dyes or pesticides by generating hydroxyl radicals or free active radicals [20-22]. Furthermore, the electron smoke on the surface of the magnetic material may be the key component in the catalytic process to enhance the photo-catalytic practices in two ways: (i) the electron smoke acts as a polarised surface because of the local electric field; (ii) the rate of recombination may be significantly shortened by trapping these carriers in the electron smoke, which creates the catalyst-dye interface needed to break down the MB dye or organic pollutants from the water. The hydroxyl or free radicals (O_2^-, ^-OH, etc.) that are generated during the glibness of e^--h^+ couples via H_2O and O_2 function as an active species in photon-induced catalysis.

In the photo-catalytic process, the hydroxyl radicals or free radicals (O_{2-}, ^-OH, etc.) that are generated during the glibness of electron-hole pairs via water and oxygen function as energetic species:

$$Mg/ZnO + Photon = Mg/ZnO^* (formation\ of\ e^- - h^+)$$

$$Mg^{3+} + e^- = Mg^{2+}\ (e^-\ trap)$$

$$O_2 + Mg^{2+} = Mg^{3+} + O_2^-$$

$$O_2^- + H^+ = \cdot OOH$$

$$\cdot OOH + e^-_{CB} + H^+ = H_2O_2$$

$$e^-_{CB} + H_2O_2 = \cdot OH + {}^-OH\ (creation\ of\ Hydroxyl\ radical)$$

$$h^+_{CB} + MB = Dye\ Oxidized$$

A non-toxic or innocuous substance is formed when this hydroxyl radicals/free radicals combine with the organic impurities in MB dye during the dye breakdown process.

$$^{\cdot}OH + MB\ Dye = CO_2 + H_2O$$

$$^{\cdot}O_2^- + MB\ Dye = H_2O + CO_2$$

It is evident from this action that pure ZnO's photocatalytic activity is significantly increased upon the addition of Mg doping content.

Conclusion

The Mg doped ZnO sample was successfully created at 450 ˚C using the co-perception technique in order to investigate

the effects of Mg ions on the preparation process and its properties. The wurtzite hexagonal structure is verified by the XRD data. The computed values for the Mg doped ZnO crystallite sizes, planner distance, and cell volume are 35.2 nm, 2.6122 Å, and 60.91 $Å^3$. Agglomeration in ZnO may be seen in the FESEM photos of Mg doped ZnO. The emission wavelength (λ) is observed to be approximately 450 nm from the PL graph. The peaks in the IR spectra are located between 520 and 640 cm^{-1}, and they correspond to the Zn-O bond being stretched. Using a photocatalytic reactor, the photocatalytic degradation of magnesium-doped ZnO nanoparticles was measured for two hours. The sample of Mg-doped ZnO has a degradation efficiency (η%) of 67%, indicating its potential utility in the dye industry for purifying water.

Acknowledgement

Authors are thankful to the Department of Physics, Baba Mastnath University, Rohtak (India) for providing facilities.

References

1. M. Caglar, S. Ilican, and Y. Caglar, Influence of dopant concentration on the optical properties of ZnO: In films by sol–gel method, Thin Solid Films 517, no. 17 (2009), 5023-5028.

2. K. H. Kim, Z. Jin, Y. Abe, and M. Kawamura, A comparative study on the structural properties of ZnO and Ni-doped ZnO nanostructures, Materials Letters 149 (2015), 8-11.

3. A Mclaren, T. V. Solis, G. Li, and S. C. Tsang, Shape and size effects of ZnO nanocrystals on photocatalytic activity, Journal of the American Chemical Society 131, no. 35 (2009), 12540-12541.

4. J. Schrier, D. O. Demchenko, and A. P. Alivisatos, Optical properties of ZnO/ZnS and ZnO/ZnTe heterostructures for photovoltaic applications, Nano letters 7, no. 8 (2007), 2377-2382.

5. A. S. Menon, N. Kalarikkal, and S. Thomas, Studies on structural and optical properties of ZnO and Mn-doped ZnO nanopowders, Studies 1, no. 2 (2013).

6. M. Kumar, V. Bhatt, R. A. Abhyankar, J. Kim, A. Kumar, and J. H. Yun, Modulation of structural properties of Sn doped ZnO for UV photoconductors, Sensors and Actuators A: Physical 270 (2018), 118-126.

7. M. Ghorbani, M. R. Golobostanfard, and H. Abdizadeh, Flexible freestanding sandwich type ZnO/rGO/ZnO electrode for wearable supercapacitor, Applied Surface Science 419 (2017), 277-285.

8. M. Shafiq, T. Yasin, M. A. Rafiq, and Shaista, Structural, thermal, and antibacterial properties of chitosan/ZnO composites, Polymer composites 35, no. 1 (2014), 79-85.

9. M. Sreejesh, S. Dhanush, F. Rossignol, and H. S. Nagaraja, Microwave assisted synthesis of rGO/ZnO composites for non-enzymatic glucose sensing and supercapacitor applications, Ceramics International 43, no. 6 (2017), 4895-4903.

10. N. Saha, A. K. Dubey, and B. Basu, Cellular proliferation, cellular viability, and biocompatibility of HA-ZnO composites, Journal of Biomedical Materials Research Part B: Applied Biomaterials 100, no. 1 (2012), 256-264.

11. S. Wang, S. Ge, and D. Zhang, Comparison of tribological behavior of nylon composites filled with zinc oxide particles and whiskers, Wear 266, no. 1-2 (2009), 248-254.

12. Z. Xiang, J. Zhong, S. Huang, J. Li, J. Chen, T. Wang, M. Li, and P. Wang, Efficient charge separation of Ag2CO3/ZnO composites prepared by a facile precipitation approach and its dependence on loading content of Ag2CO3, Materials Science in Semiconductor Processing 52 (2016), 62-67.

13. Z. Li, Improving the electric field distribution in stress cone of HTS dc cable terminals by nonlinear conductive epoxy/ZnO composites, IEEE Transactions on Applied Superconductivity 29.2 (2018), 1-5.

14. H. M. Cao, Z. Liu, T. Liu, S. Duo, L. Huang, S. Yi, and L. Cai, Well-organized assembly of ZnO hollow cages and their derived Ag/ZnO composites with enhanced photocatalytic property, Materials Characterization 160 (2020), 110125.

15. B. Shohany and A. K. Zak, Doped ZnO nanostructures with selected elements-Structural, morphology and optical properties: A review, Ceramics International 46.5 (2020): 5507-5520.

16. S. Suwanboon, P. Amornpitoksuk, and A. Sukolrat, Dependence of optical properties on doping metal, crystallite size and defect concentration of M-doped ZnO nanopowders (M= Al, Mg, Ti), Ceramics International 37, no. 4 (2011), 1359-1365.

17. B. Y. Geng, G. Z. Wang, Z. Jiang, T. Xie, S. H. Sun, G. W. Meng, and L. D. Zhang, Synthesis and optical properties of S-doped ZnO nanowires, Applied Physics Letters 82, no. 26 (2003), 4791-4793.

18. J. Yang, M. Gao, L. Yang, Y. Zhang, J. Lang, D. Wang, Y. Wang, H. Liu, and H. Fan, Low-temperature growth and optical properties of Ce-doped ZnO nanorods, Applied Surface Science 255, no. 5 (2008), 2646-2650.

19. A. Hameed, T. Montini, V. Gombac, and P. Fornasiero, Photocatalytic decolourization of dyes on NiO–ZnO nano-composites, Photochemical & Photobiological Sciences 8 (2009), 677-682.

20. G. Di, Z. Zhu, Q. Huang, H. Zhang, J. Zhu, Y. Qiu, D. Yin, and J. Zhao, Targeted modulation of g-C3N4 photocatalytic performance for pharmaceutical pollutants in water using ZnFe-LDH derived mixed metal oxides: Structure-activity and mechanism, Science of The Total Environment 650 (2019), 1112-1121.

21. W. A. Sadik, O. M. Sadek, and A. M. Demerdash, The Use of heterogeneous advanced oxidation processes to degrade neutral Red Dye in aqueous solution, Polymer-Plastics Technology and Engineering 43, no. 6 (2004), 1675-1686.

22. Q. Wan, T. H. Wang, and J. C. Zhao, Enhanced photocatalytic activity of ZnO nanotetrapods, Applied Physics Letters 87, no. 8 (2005).

23. Y. H. Tan, K. Yu, J. H. Li, H. Fu, and Z. Zhu, MoS2@ ZnO nano-heterojunctions with enhanced photocatalysis and field emission properties, Journal of Applied Physics 116, no. 6 (2014).

24. K. Hayat, M. A. Gondal, M. M. Khaled, S. Ahmed, and A. M. Shemsi, Nano ZnO synthesis by modified sol gel method and its application in heterogeneous photocatalytic removal of phenol from water, Applied Catalysis A: General 393, no. 1-2 (2011), 122-129.

25. S. Payra, S. K. Ganeshan, S. Challagulla, and S. Roy, A correlation story of syntheses of ZnO and their influence on photocatalysis, Advanced Powder Technology 31, no. 2 (2020), 510-520